Optimization of Moving Coil Actuators for Digital Displacement Machines

Nørgård, Christian; Bech, Michael Møller; Roemer, Daniel Beck; Pedersen, Henrik Clemmensen

Published in:
Proceedings of the 8th Workshop on Digital Fluid Power (DFP16)

Publication date:
2016

Document Version
Accepted author manuscript, peer reviewed version

Peer-reviewed version

OPTIMIZATION OF MOVING COIL ACTUATORS FOR DIGITAL DISPLACEMENT MACHINES

Christian Noergaard, Michael M. Bech, Daniel B. Roemer, Henrik C. Pedersen
Department of Energy Technology
Aalborg University
Pontoppidanstraede 111, 9220 Aalborg East, Denmark
E-mail: {chn,mmb,dbr,hcp}@et.aau.dk

ABSTRACT

This paper focuses on deriving an optimal moving coil actuator design, used as force producing element in hydraulic on/off valves for Digital Displacement machines. Different moving coil actuator geometry topologies (permanent magnet placement and magnetization direction) are optimized for actuating annular seat valves in a digital displacement machine. The optimization objectives are to the minimize the actuator power, the valve flow losses and the height of the actuator. Evaluation of the objective function involves static finite element simulation and simulation of an entire operation cycle using a single chamber Digital Displacement lumped parameter model. The optimization results shows that efficient operation is achievable using all of the proposed moving coil geometries, however some geometries require more space and actuator power. The most appealing of the optimized actuator designs requires approximately 20 W on average and may be realized in 20 mm $\times$ Ø 22.5 mm (height $\times$ diameter) for a 20 kW pressure chamber. The optimization is carried out using the multi-objective Generalized Differential Evolution optimization algorithm GDE3 which successfully handles constrained multi-objective non-smooth optimization problems.

KEYWORDS: Moving Coil Actuator, Digital Fluid Power, Digital Displacement Machines, Multi-Objective Optimization, Digital Hydraulic Valves

1 INTRODUCTION

Digital Displacement Machines (DDM's) are a promising new topology which relies on several pressure chambers being connected to a high- and low-pressure manifold through two on/off valves, controlled on a stroke-by-stroke basis. For the machine operation to be efficient, the valves must be fast switching, leakage free, induce a low pressure drop and the actuators must be efficient. To this end, direct electro-magnetic actuators are typically used in combination with an annular seat valve [1] in an integrated and compact mechatronic valve design. Annular seat valves features a large discharge area relative to the stroke length which, facilitates both fast switching and lower pressure losses during valve

flow (compared against spool valves). The most widespread electro-magnetic actuators in fluid power are solenoids, as they feature a simple and robust design. However, the transient performance suffers from an inherent magnetic diffusion delay and are non-linear in nature making them complicated to control. MC actuators possess some desirable features and characteristics e.g. rapid fast force response, typically they have linear current to force characteristics and they facilitate bi-directional force capability [2]. Still, MC actuators are not widespread in hydraulics, and the research published on their performance is limited. The nature of the DDM operation make great demands to the robustness of the actuators and valves, as they must be durable for large number cycles, and furthermore, the moving member is exposed to high and fluctuating pressure levels. To verify the simulation models used in the optimization and to test the mechanical robustness, a valve and actuator prototype has been produced based on the optimization results presented in this paper. The valve and actuator prototype are shown in Fig. 1. In the near future the valve prototype is to be installed in a hydraulic radial piston machine which has been modified to accommodate DDM operation.

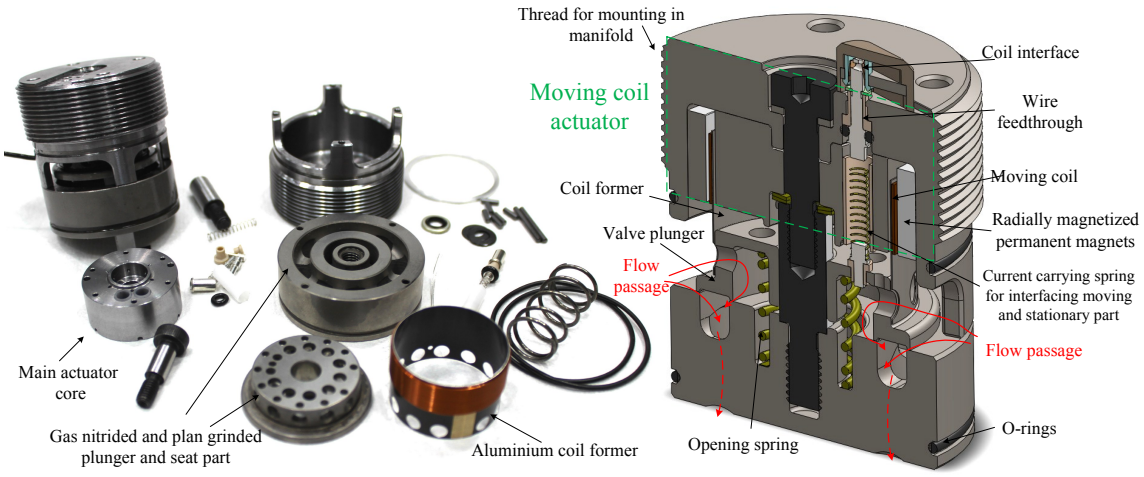

Figure 1: Illustrations of the valve and the actuator prototype.

To evaluate the performance of a MC actuator design, a number of simulation models are used, incl. static electro-magnetic finite-element analysis (FEA) and lumped parameter time dependent simulation, which facilitates simulation of entire DDM operation cycles. The FEA enables accurate estimates of important actuator parameters while the lumped model enables simulation of the machines performance when imposing different operating conditions.

The paper is organized as follows: Section 2 provides some background information on DDM's, electro-magnetic actuators, and the GDE3 optimization algorithm. Section 3 explains the mathematical models used to evaluate the optimization objectives. Section 4 presents how the optimization problem is formulated and Section 5 presents and discusses the optimization results. Finally, some conclusions are drawn based on the optimization results in Section 6.

2 BACKGROUND

The Digital Displacement technology was invented at the University of Edinburgh, and later spun off in the company Artemis Intelligent Power Ltd. The first patent for the Digital Displacement pump was filed in 1989 [3], followed by the Digital Displacement motor in 1990 [4]. In 2011 Mitsubishi Heavy Industries announced plans for testing a wind turbine in the 7 MW class where the drivetrain is based on the Artemis technology, but detailed information is still not published [5]. Although no detailed information is available regarding valve performance or design specifications, the valves installed in the machine appear to be direct actuated seat valves, with a variable reluctance actuator (solenoid) as the force producing element, based on graphics included in the patent applications [6, 7, 8].

Several different electro-magnetic actuator topologies exist which may be utilized as the force producing element in the fast switching valves of DDM's. Feasible topologies include variable reluctance actuators (solenoids) [9], polarized variable reluctance actuators [10], moving magnet actuators [11], and MC actuators (voice coils) [12]. However, since all of these electro-magnetic actuator topologies are feasible for use as DDM valve actuator, it is not apparent which topology is the most suited for the application. In [2] the suitability of different actuator topologies applied in DDM's is analysed revealing the moving magnet actuator to exhibit superior performance characteristics.

Differential Evolution (DE) algorithms are a relatively new class of Evolutionary Algorithms. It has gained popularity since it has proven to be capable of solving difficult multi-objective optimization problems successfully. The DE algorithm, which GDE is an extension of, was introduced by Storn and Price in 1995 [13]. The key benefits of the DE algorithm, when first introduced, were its simplicity, efficiency and a low number of optimization control variables. The algorithm used to carry out the optimization is referred to as Generalized Differential Evolution 3 (GDE3). GDE3 improves earlier GDE versions in the case of multiple objectives by giving a better distributed solution [14]. The GDE3 uses Pareto optimization i.e. the algorithm returns a set of solutions which are non-dominated by any other solution. The GDE3 algorithm uses weak-constraint domination which means the degree of constraint violation should be expressed in the constraint functions. This accelerates the convergence of the algorithm since designs with a high degree of constraint violation is opted out through comparison and pruning schemes [15].

3 MODEL FRAMEWORK

The model framework comprises two distinct models which are executed sequentially. Firstly, a static electro-magnetic FEA is carried out based on a specified actuator geometry, and secondly a lumped parameter DDM simulation model is executed. The FEA enables calculation of important actuator parameters based on the solution of the initial magnetic field induced by the permanent magnets of the MC actuator. The lumped parameter DDM model simulates the entire operation cycle using the parameters obtained from the FEA, some DDM parameters and some predetermined DDM operating conditions. The following sub-sections describe the main details of both simulation models.

3.1 Static Electro-Magnetic Finite-Element-Analysis

The problem is modelled as an axi-symmetric problem since the actuator geometry primary is primarily rotation-symmetric. The model is simulated using the open-source software FEMM v.4.2 scripted through Matlab. The software returns a solution to the initial magnetic field generated by the permanent magnets which satisfies both expressions of Eq. 1 via a magnetic vector potential approach [16].

$$\nabla \cdot \overrightarrow{B} = 0 \qquad \nabla \times \overrightarrow{H} = \overrightarrow{J} \tag{1}$$

where $\overrightarrow{H}$ is the field intensity and $\overrightarrow{B}$ is the flux density. The field intensity and flux density are related through the permeability μ. The advantage of solving for the magnetic vector potential is that all the conditions to be satisfied can be combined into a single equation. By rewriting the flux density as $\overrightarrow{B} = \nabla \times \overrightarrow{A}$, where $\overrightarrow{A}$ is the magnetic vector potential, both expressions in Eq. 1 can be combined to Eq. 2. For the general 3-D case $\overrightarrow{A}$ is a vector with three components. However, in the axi-symmetric case two of these components are zero which reduces the computational effort needed to solve the model significantly.

$$\nabla \times \left(\frac{1}{\mu\left(\overrightarrow{B}\right)} \nabla \times \overrightarrow{A} \right) = \overrightarrow{J} \tag{2}$$

To solve Eq. 2 magnetic and electrical properties must be specified for all materials used in the model. The materials properties used in the model are given in Tab. 1. Fig. 2 shows measured hysteresis loops for low carbon steel used as core material.

Table 1: Magnetic and electrical properties of materials used in static electro-magnetic FEA.

Material	**BH-relation [A/m,T]**	**Conductivity [S/m]**
Air	$\mu_r = 1$	0
Copper (@100°C)	$\mu_r = 1$	$4.55 \cdot 10^7$
Magnet (NeFeB 35MGOe)	$\mu_r = 1.045$, $H_c = 9.15 \cdot 10^5$	0 (shell magnets)
Low carbon steel (11SMnPb30)	see Fig. 2	$5.8 \cdot 10^6$
Cast steel	Selected points:*(H,B)*={(0,0)(1.15k,1.11), (1.73k,1.27), (4.08k,1.53),(16.93k,1.87)}	$6.20 \cdot 10^6$

Based on the (specified) actuator geometry input, the regions are defined with the appropriate properties. Additional to the regions given by the actuator geometry a surrounding air domain is included with asymptotic boundary conditions to emulate an open space. Each region of the solution domain is meshed using the software's auto-mesh method which typically results in a mesh consisting of 2500 to 5000 triangular elements. The initial magnetic flux distribution, using the geometry of the derived optimal design used for the valve prototype, is shown in Fig. 4 along with the generated mesh.

The average total field intensity at the core steel boundary adjacent to the air gap and the average radial flux density in the air gap, indicated in Fig. 4, are extracted from the FEA results to calculate the MC actuator parameters. These quantities, along with an estimate of static inductance, are used in the dynamic lumped actuator model explained in Section 3.2.

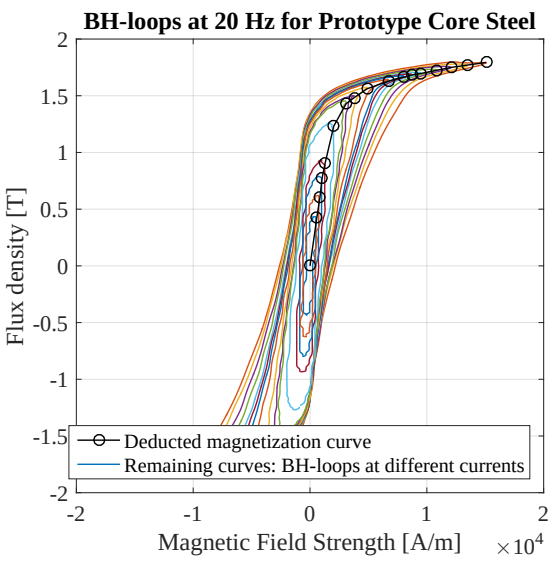

Figure 2: Measured hysteresis BH-curves, using the approach given in [17], for the steel used in the prototype with the deducted BH-curve used in the FEA.

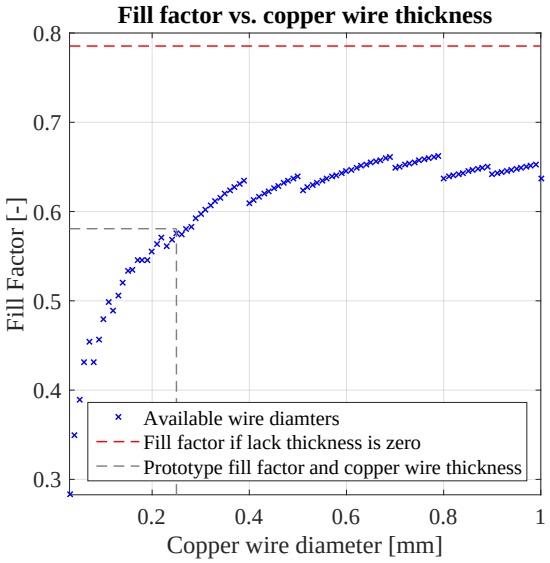

Figure 3: Achievable fill factor as a function of copper wire diameter. Data based on available wires at voice coil manufacturer Nikkei Electric Co., LTD.

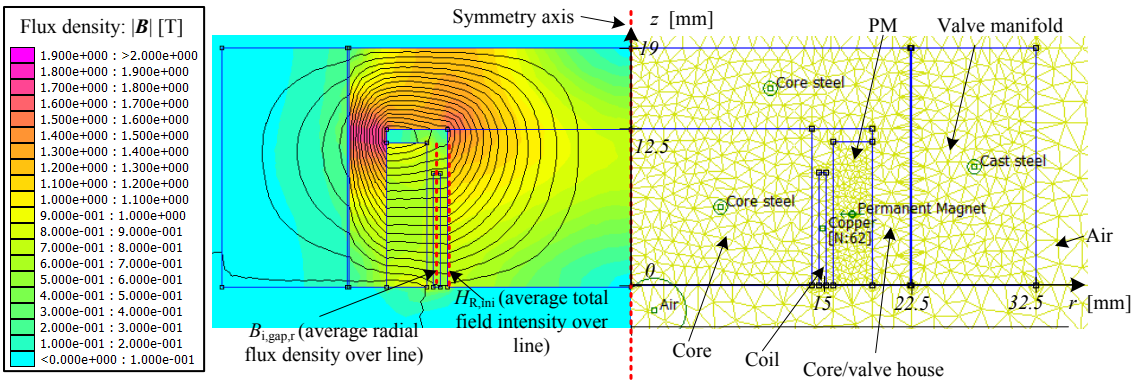

Figure 4: Auto generated mesh consisting of 3238 triangular elements and the initial magnetic flux distribution generated by the permanent magnets for the prototype actuator.

The coil fill factor used in the FEA and optimization is incorporated as a discrete function of the wire thickness as shown in Fig. 3. This is done to account for the poor achievable fill factor when using thin wires. The data is based on the available wire thickness (and resulting insulation lack layer) from the coil manufacturer used for the valve prototype.

3.2 Lumped Parameter Digital Displacement Machine Simulation Model

A lumped parameter model for a single pressure chamber of a DDM has been constructed which facilitates simulation of entire machine cycles under various operating conditions. The model comprises several sub-models, which each seek to describe specific energy exchanges that happen within a DDM. The sub-models of the DDM simulation model interact as shown in Fig. 5. The driving input is the movement of the shaft from which the movement of the piston in the pressure chamber is obtained. By imposing appropriate initial conditions and manipulating the valve control signals at appropriate times, according to the piston position, the model facilitates simulation of all three operation cycles i.e.

motoring, pumping and idling. However for the optimization problem at hand only the motoring cycle is used. During simulation, several internal transient states of the DDM are solved e.g. pressures, flows, plunger dynamics, actuator currents etc. From analysis of the transient states important measures on performance and efficiency can be evaluated.

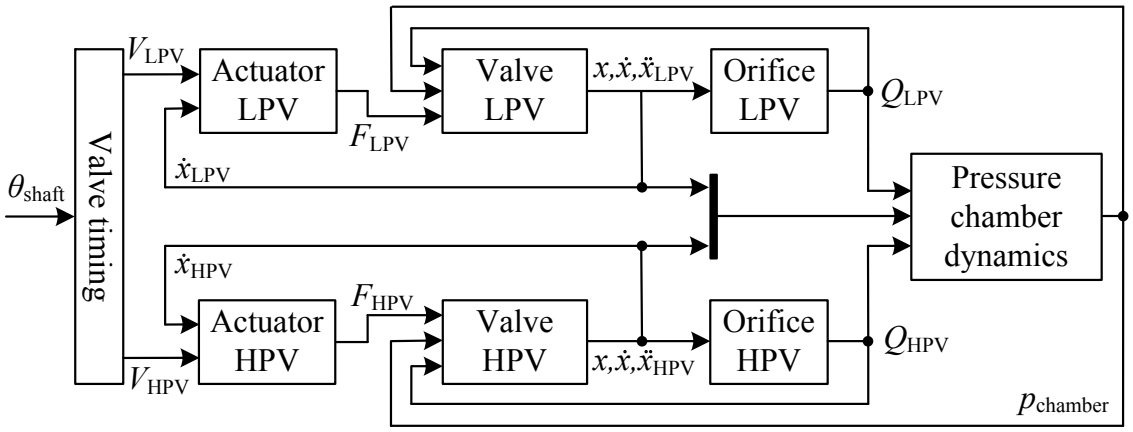

Figure 5: Block diagram showing how the different sub-models of the lumped parameter simulation model interacts.

This section focuses on the sub-models that has dominating influence on the valve and actuator related losses. These sub-models are a lumped MC actuator model, a valve dynamics model, and a flow restriction model (flow vs- pressure characteristics).

Moving Coil Lumped Parameter Actuator Model

The MC electrical dynamics is modelled using an analytical transformer model with an air gap and a primary- and secondary coil, see Fig. 8. The primary coil is the MC of the actuator and the secondary coil is a modelling element which accounts for the eddy currents generated in the core upon a change in flux density. This approach was suggested in [18], and in [19] a method to extend the approach to include non-linear magnetic diffusion effects was presented by the authors. The secondary coil parameters are based on an estimation of the magnetic field depth as a function of time [20]. The diffusion depth is defined as illustrated in Fig. 6 and Eq. 3 gives an expression for the magnetic diffusion depth.

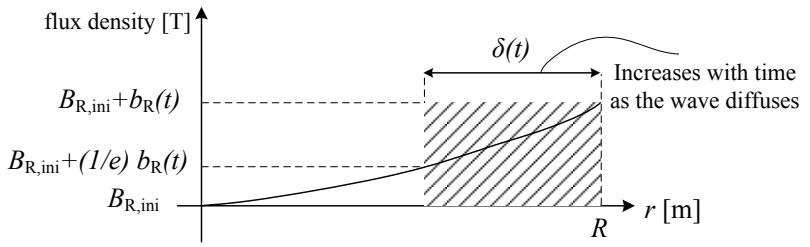

Figure 6: Illustration of the rectangular profile approximation. The radial integral of a diffusing wave is approximated by the flux density $B_{R,ini}$ at the boundary of the inner yoke material and the characteristic penetration depth $\delta(t)$.

$$\delta(t) = \delta^{(0)}(t) + \frac{\left(\delta^{(0)}(t)\right)^2}{6R} \text{ where : } \delta^{(0)}(t) = \sqrt{\frac{2\int_0^t h_{\mathrm{R}}(t)dt}{\sigma b_{\mathrm{R}}(t)}} \tag{3}$$

R is the inner core radius, h_{R} and b_{R} are the magnetic field strength and flux density change, due to coil current transients, at the boundary of the inner core (see Fig. 4). h_{R} and b_{R} are related through the obtained BH-curve data of Fig. 2, with the offset $H_{\mathrm{R,ini}}$ and $B_{\mathrm{R,ini}}$ respectively. By considering the magnetic path of the flux generated by the current as a number of reluctances connected in series, h_{R} may be calculated as [19].

$$h_{\mathrm{R}} = \frac{Ni_{\mathrm{coil}}}{l_{avg}} - \frac{Ni_{\mathrm{eddy}}}{l_{avg}} - \frac{b_{\mathrm{gap,r}} l_{\mathrm{gap}}}{l_{\mathrm{avg}}}\mu_0 - \frac{b_{\mathrm{PM}} l_{\mathrm{PM}}}{l_{\mathrm{avg}}\mu_0\mu_{\mathrm{r,PM}}} \tag{4}$$

The flux density change $b_{\mathrm{gap,r}}$ and b_{PM}, due to the coil current, is calculated based on an estimate of the flux generated by the coil current. The flux is calculated based on the diffusion depth, and the calculated flux density at the boundary of the inner core as (rectangular profile approximation):

$$\phi_{\mathrm{coil}} = A_{\mathrm{z}}\left(\delta(t)\right) b_{\mathrm{R}} \tag{5}$$

A_{z} ((t)) is the axial cross sectional area the flux passes through which varies with the diffusion depth, see Fig. 7. $b_{\mathrm{gap,r}}$ and b_{PM} are calculated from the coil flux and their cross sectional areas normal to the flux.

$$b_{\mathrm{gap}} = \frac{\phi_{\mathrm{coil}}}{A_{\mathrm{r,gap}}} \qquad b_{\mathrm{PM}} = \frac{\phi_{\mathrm{coil}}}{A_{\mathrm{r,PM}}} \tag{6}$$

$A_{\mathrm{r,gap}}$ and $A_{\mathrm{r,PM}}$ are the radial cross sectional areas which the flux passes through. Based on the diffusion depth, parameters of the two winding transformer model is continuously estimated. The eddy current resistance R_{eddy} and the eddy current paths leakage inductance L_{eddy} are calculated as:

$$R_{\mathrm{eddy}} = \frac{l_{\mathrm{eddy}}}{h_{\mathrm{coil}}\delta(t)\sigma} \qquad L_{\mathrm{eddy}} = N^2\frac{\mu_0\mu_r A_{\mathrm{z}}\delta(t)}{h_{\mathrm{coil}}} \tag{7}$$

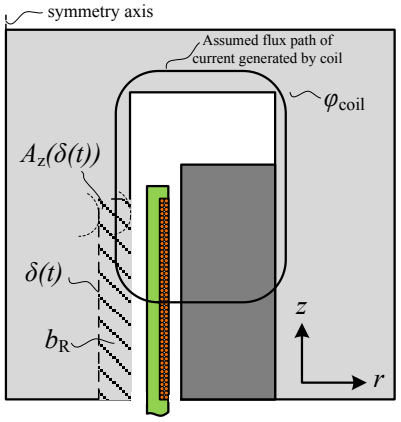

Figure 7: Sketch showing the assumed flux path of the flux generated by the coil current.

Fig. 8 illustrates the transformer model applied to the MC actuator and the equivalent magnetic circuit diagram. The governing equations, derived from the equivalent magnetic

circuit diagram are given in Eq. 8 and 9 where the shorted turn winding parameters have been referred to the coil winding:

$$v_{\text{coil}} = R_{\text{coil}} i_{\text{coil}} + (M + L_{\text{coil}}) \frac{di_{\text{coil}}}{dt} - M \frac{d(i_{\text{eddy}}/N)}{dt} - \underbrace{\dot{x} l_{\text{avg,wire}} N B_{\text{i,gap,r}}}_{\varepsilon} \tag{8}$$

$$0 = N^2 R_{\text{eddy}}(t)(i_{\text{eddy}}/N) - M \frac{di_{\text{coil}}}{dt} + (M + L_{\text{eddy}}(t)) \frac{d(i_{\text{eddy}}/N)}{dt} \tag{9}$$

where v_{coil} is the coil voltage, R_{coil} is the coil resistance (incl. current carrying spring- and wire feedthrough resistance), M is the mutual inductance linking both the main eddy current path and the coil, L_{coil} and L_{coil} is the leakage inductance of the coil and the eddy current path respectively, N is the number of coil turns, $\dot{x}$ is the velocity of the coil, $l_{\text{avg,wire}}$ is the average length of a single wire turn, i_{coil} and i_{eddy} is the coil current and the eddy current magnitude respectively. The generated magnetic Lorentz force is calculated as:

$$F_{\text{act}} = i_{\text{coil}} B_{\text{i,gap,r}} l_{\text{avg,wire}} N \tag{10}$$

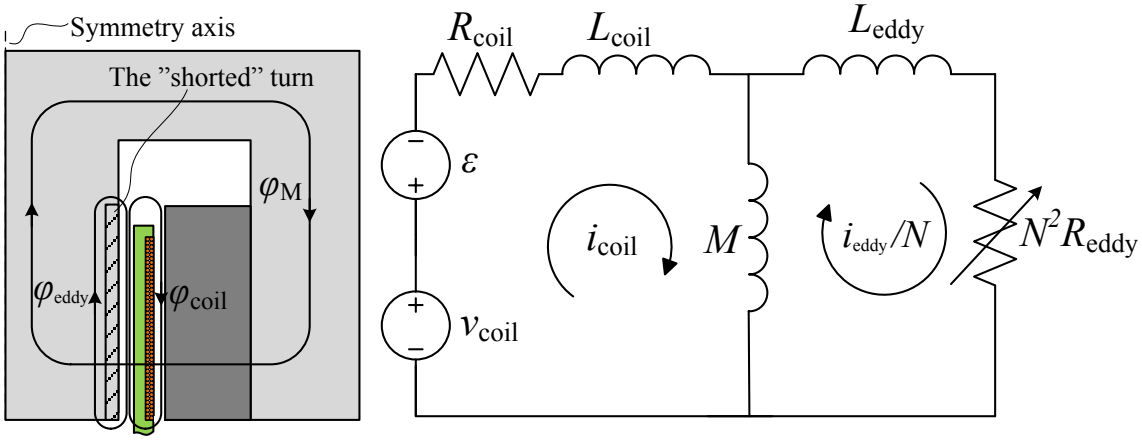

Figure 8: Transformer model applied to MC actuator and equivalent magnetic circuit diagram where the shorted turn parameters are referred to the coil side.

Modelling of Valve Plunger Dynamics

When leading flow through semi-opened valves the flow losses are considerable. In addition, the optimization results reveal the that the actuators should be relatively weak actuators. This establishes demands to the accuracy of the models since the valve movement is likely to be dominated by the flow- and movement induced fluid forces acting on the plunger during switching. While the models must give accurate and reliable characteristics they should still be computational efficient to keep the computational burden at a manageable level.

Since only the actuator of the valve is to be optimized in this design step, the plunger geometry is fixed. The flow and movement dependent parameters are obtained through CFD simulations, in [21] and are used in the lumped parameter model. The force equilibrium may be written as:

$$\ddot{x} = \frac{1}{m_{\text{moving}}} \left(F_{\text{mov}}(x, \dot{x}, \ddot{x}) + F_{\text{fluid}}(x, Q, p_{\text{c}}) + F_{\text{act}}(i_{\text{coil}}) + F_{\text{spring}}(x) \right) \tag{11}$$

Where F_{mov} is the movement-induced fluid force, F_{fluid} is the flow- and pressure-induced fluid force, F_{act} is the electro-magnetic actuator force and $F_{\text{spring}}$is the opening spring force. In addition to the force contributions shown in Eq. 11 a suitable end-stop model have been implemented which limits the plunger position within the confines of the actuator stroke-length and resets the plunger acceleration and velocity accordingly.

Movement-Induced Fluid Force Model

The movement-induced fluid force arises as the valve moving member is forced through the surrounding fluid whereby the surrounding fluid is forced to displace. This force contribution is often neglected in non-CFD models due to the complexity of describing this force for general valve geometries. For fast switching valves with large shadow areas this force contribution may be significant [22, 23].

Generally, the force exerted on a rigid body moving through a fluid domain is governed by the Navier-Stokes equation. Analytical solutions to this problem is limited to simple cases, they may however still be useful for gaining insight to the governing characteristics for more complicated geometries. The model is derived based on an analytic solution to the Navier-Stokes equation for a sphere moving in a linear path through an otherwise stationary fluid [24]. The used model, proposed in [21] is shown in Eq. 12 where the parameters k_{a}, k_{v}, k_{d}, k_{h} are determined using CFD analysis.

$$F_{mov} = \underbrace{k_{\text{a}}(x)\ddot{x}}_{Added\,mass\,term} - \underbrace{k_{\text{v}}(x)\dot{x}}_{Viscous\,term} - \underbrace{k_{\text{d}}|\dot{x}|\dot{x}}_{Drag\,term} - \underbrace{k_{\text{h}}\int_0^t \frac{d\dot{x}}{d\tau}\frac{1}{\sqrt{t-\tau}}d\tau}_{History\,term} \tag{12}$$

In order to simulate the movement-induced fluid forces using Eq. (12), the history term must be -reformulated to a form appropriate for discrete time domain simulation. Assuming piece-wise constant acceleration, the history term may be approximated using:

$$k_{\text{h}}\int_0^t \frac{d\dot{x}}{d\tau}\frac{1}{\sqrt{t-\tau}}d\tau \tag{13}$$
$$= 2k_{\text{h}}\left(\left.\frac{d\dot{x}}{dt}\right|_{T_1}(\sqrt{t}-\sqrt{t-T_1}) + \left.\frac{d\dot{x}}{dt}\right|_{T_2}(\sqrt{t-T_1}-\sqrt{t-T_2}) + \ldots + \left.\frac{d\dot{x}}{dt}\right|_{T_{\text{f}}}(\sqrt{t-T_{\text{f}-1}}-\sqrt{\text{t}-\text{T}_{\text{f}}})\right)$$

Where sampling times are denoted $t = \{T_1, T_2, \ldots, T_{\text{f}}\}$. The above expression increases in size during simulation, and all previous accelerations and the corresponding time stamps must be assessable during simulation. Evaluation of the history term is relatively time consuming, especially after some time as the number of samples increases. To circumvent this and keep the computational burden at a manageable level, the history term is only evaluated during valve movement, and the number of sampling times in the evaluation is kept at a fixed and manageable number. More details on derivation of the movement-induced fluid forces and model verification are presented in [21].

Flow and Pressure Induced Forces

The flow force F_{flow} is modelled as:

$$F_{\text{flow}} = k_{\text{f1}}(x)Q^2 + k_{\text{f2}}(x)Q \tag{14}$$

Where k_{f1} and k_{f2} are functions of the valve plunger position fitted through CFD analysis (details in [21]). When the valve is closed $(x = 0)$, a switched condition is used to account for the force induced by the pressure difference across the valve:

$$F_{\text{fluid}} = \begin{cases} F_{\text{flow}} & x > 0 \\ A_s \Delta p & x = 0 \end{cases} \tag{15}$$

Where A_s is the axial shadow area of the valve plunger and Δp is the pressure difference across the valve.

Flow vs. Pressure Loss Model

The pressure loss during valve flow must be modelled with a relatively large degree of accuracy since the associated energy loss is significant. The used model aims to model the relation between flow and pressure for a wide range of flow rates and for complicated valve geometries. The used model was proposed in [25] and showed good accuracy for a wide range of flow rates:

$$\Delta p = k_{p1}(x)Q^2 + k_{p2}(x)Q \tag{16}$$

where k_{p1} and k_{p2} are functions of the valve position determined through a number of CFD simulations.

3.3 Objective Function Evaluation

All of the objectives used in the optimization are calculated using the described simulation models. Depending on the specified design vector, some constraints could be violated during execution of the static FEA model. In this case, the lumped parameter simulation model is not executed to reduce the computational time. Similarly, execution of the lumped parameter simulation model is omitted if the actuator force at steady current does not exceed the opposing spring force the actuator must overcome to initiate movement. Figure 9 illustrates how the objective function is evaluated. The bold face letters represents the constraint and objective functions, which are additional explained in Section 4.

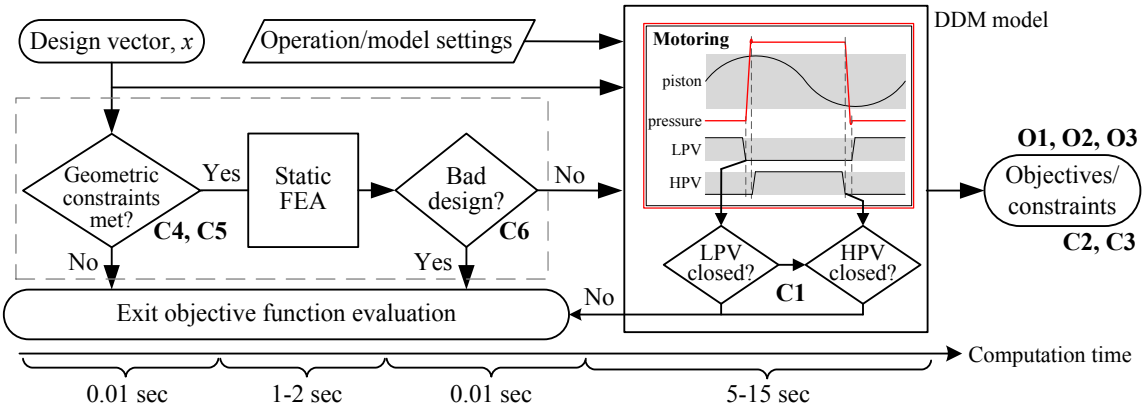

Figure 9: Flow chart illustrating how the objective function is evaluated.

In addition to the efforts made to reduce the computational time several designs are evaluated simultaneously. This is realized by using a workstation PC with 16 GB ram and 8 cores, each optimized for running dual threads, leaving 16 threads at disposal for parallel processing of the objective function.

3.4 Simulation Example of Model

Fig. 10 shows a simulation example of the lumped parameter DDM model, using the optimized prototype design and the operating conditions given in Tab. 2. The valves are actively closed by a rapid response of the MC actuator while the valve opening occurs passively due to pressure and spring forces.

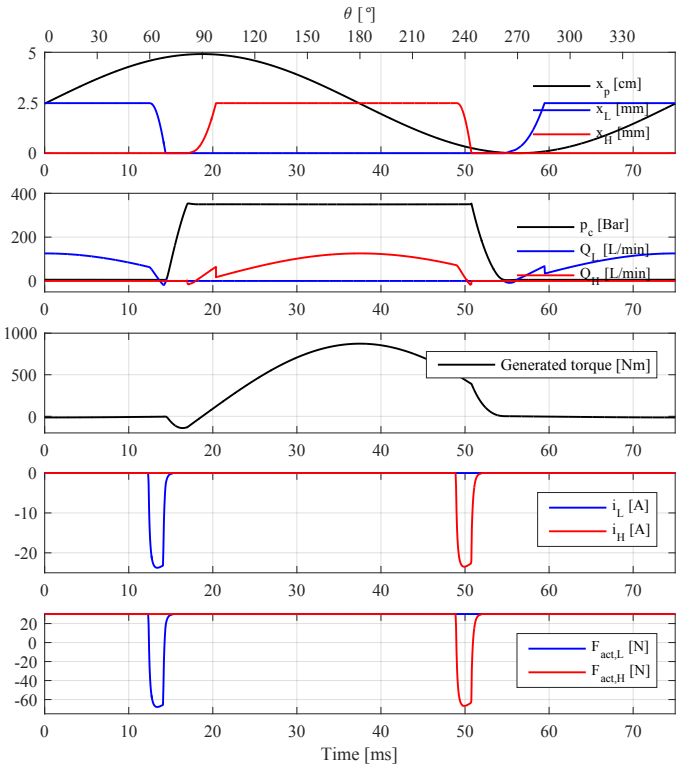

DDM parameters	**Value**
Piston stroke length	49 mm
Piston bore Ø	36mm
Cylinder dead volume	62 CC
Displacement[1]	50 CC/rev
Prototype valve par.	
Stroke length, l_{stroke}	2.5 mm
Shadow area, A_s	4.9 cm^2
spring preload, L/H	(30/30)N
Coil Layers	2
Operating cond.	
Shaft speed	800 RPM
Supply pressure, L/H	(5/350) bar
Supply voltage	80 V
Performance data	
Avg. act. power, L/H	(21/21)W
Avg. flow loss, L/H	(25/25)W
L/H closing time	(2.1/1.9) ms
L/H opening time	(3.1/3.3) ms
Avg. power[1]	22 kW
Cycle efficiency[2]	99.4%

Figure 10 & Table 2: Simulation example using the prototype actuator design and DDM parameters and operation conditions given in the table.

4 FORMULATION OF THE OPTIMIZATION PROBLEM

The valves should be fast switching to minimize the flow when the valves are semi-open. But how much actuator power should be invested to minimize the combined valve and actuator losses? In addition, typically, several valves and actuators are integrated in a compact DDM design. Therefore, size and compactness of the actuators should also be emphasized in the design. To this end, the used objectives to be minimized are:

O1 Avg. actuator power: $P_{\text{act}} = \left(\int_0^{T_{\text{cycle}}} v_{\text{L}}\, i_{\text{L}} dt + \int_0^{T_{\text{cycle}}} v_{\text{H}}\, i_{\text{H}} dt \right) \Big/ T_{\text{cycle}}$

O2 Core height: h_{core} (see Fig. 12).

O3 Avg. flow losses: $P_{\text{flow}} = \left(\int_0^{T_{\text{cycle}}} \Delta p_{\text{L}}\, Q_{\text{L}} dt + \int_0^{T_{\text{cycle}}} \Delta p_{\text{H}}\, Q_{\text{H}} dt \right) \Big/ T_{\text{cycle}}$

[2]Only valve losses considered.
[1]Only one chamber considered.

Where T_{cycle} is the cycle duration, v_{L}, v_{H}, i_{L} and i_{H} are the actuator voltages and currents, Δp_{L}, Δp_{H}, Q_{L} and Q_{H} are the valve pressure drops and flows. By minimizing these three objectives an efficient motoring operation is ensured, along with an efficient and compact actuator design.

The permanent magnet (PM) could be placed in several different positions and magnetized in different directions. The different geometries or permanent magnet placements that have been explored are shown in Fig. 11. Each of the four geometries represents an optimized design point (highlighted in Fig. 13). The PM of design **A** and **B** are radially magnetized, whereas for design **C** and **D** the PM is axially magnetized.

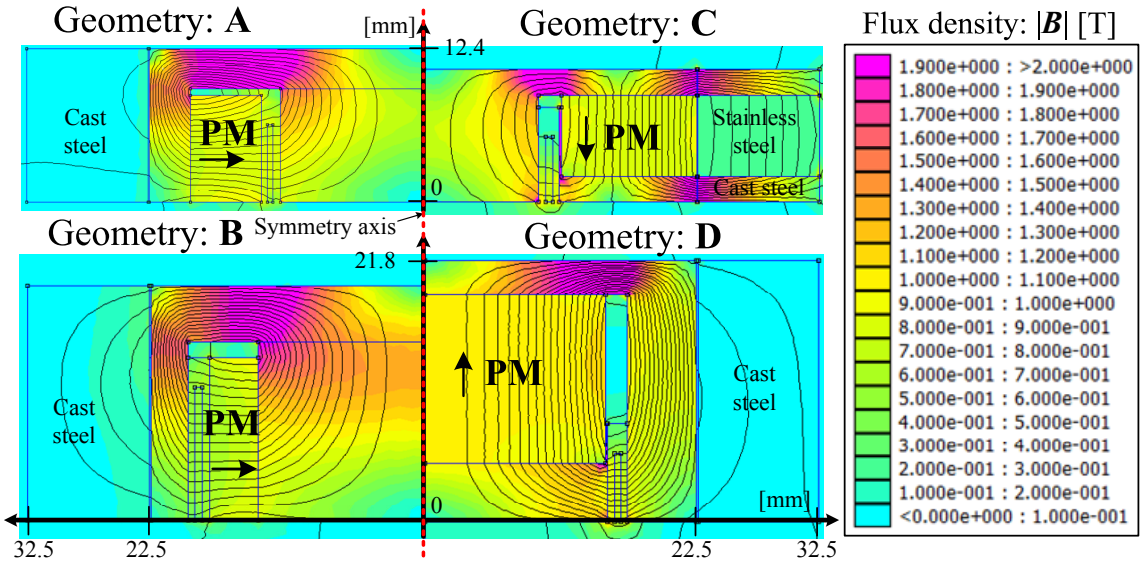

Figure 11: Overview of the different geometries that are explored in the paper. Each design is optimized and represents the highlighted points of Fig. 13.

In connection, not only performance should be considered, the design topology should also be easy to manufacture and assemble. When using axial magnetization the permanent magnet can be realized in a one solid which easily can be incorporated in the design. The radial magnetization is realized by a number of cylinder ring section shaped shell magnets, each individually magnetized (to realize sufficient flux levels during magnetization). Also, geometry **C** has a ring of stainless steel incorporated in the outer cast iron to avoid magnetic short-circuiting in the outer cast. Figure 12 shows the parametrization of geometry **C** (with a two coil layer winding), and Tab. 3 gives the design variables.

In addition to the geometry related design variables, four control related design variables are used for defining a simple modulation. The MC is excited with voltage pulses of constant amplitude. One design variable is used to determine the voltage pulse start shaft angle, and one design variable determines the duration of the corresponding voltage pulse, for each valve (see Tab. 3).

Lastly, constraint functions must be formulated. The constraint functions are formulated to express the violation degree of each constraint function to benefit from the weak constraint domination scheme of GDE3. A number of geometry related constraint functions are formulated for each of the geometries that have been tested. Additionally, constraints are used for designs that are obviously bad or simulation of the lumped parameter model did not finish successfully. The constraints used for geometry A are:

C1 Success indicator: Depending on the design point, the operation cycle may only be

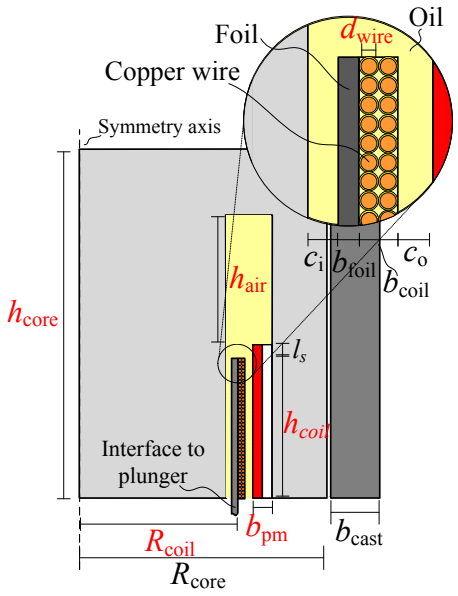

Design var.	**Description**	**Bounds**
h_{core}	Height of act. core	[0.1,1] mm
R_{coil}	Radius of coil	[5,20]mm
b_{PM}	Thickness of PM	[0,10]mm
h_{coil}	Height of coil	[3,50]mm
d_{wire}	Copper wire thickness	[0.1,1]mm
h_{air}	Height of gap above PM	[0,10]mm
V_{supply}	Supply voltage for acts.	[5,300]V
θ_L	Voltage step angle	[50,90]rad
θ_H	Voltage step angle	[230,270]rad
$\Delta\theta_L$,$\Delta\theta_H$	Voltage step duration	[1,15]rad
Geo Consts.	**Description**	**Value**
c_i,c_o	Inner and outer clearance	(0.4,0.5)mm
R_{core}	outer core radius	22.5 mm
b_{cast}	outer cast thickness	10 mm
b_{foil}	former thickness	0.2 mm

Figure 12 & Table 3: Parametrization of geometry A. The red parameters are design variables and the black parameters constants. The Table gives all design variables for geometry A along with some geometrical constants.

completed partially (too weak actuators, bad timing, etc). The violation degree is set based on the simulation time at which the operation cycle failed.

C2 Efficiency out of range: an cycle efficiency in the range 75-100 % is expected. The constraint is unsatisfied if the evaluated efficiency lies out of that range.

C3 Energy utilization constraint: the output energy should be at least half of the ideal input energy.

C4 Geometry constraint: coil height must be smaller than actuator core height.

C5 Geometry constraint: outer radius of PM must be smaller than outer core radius.

C6 Bad design indicator: magnetic force in steady state at voltage level V_{supply} must be greater than the opposing spring force.

5 OPTIMIZATION RESULTS

This section shows the optimization results obtained while using the different MC actuator geometry topologies. Fig. 13 shows the achieved Pareto fronts using the four proposed geometries while Tab. 4 gives the problem infos and solution statistics. The geometry and initial flux distribution for the highlighted design points are shown in Fig. 4 and 11. For geometry A, B and C each design point of the population are non-dominated by any other design point i.e. Pareto optimial, whereas only 30 % of the population for geometry D are non-dominated. Common for all the different geometries is the average flow loss which only varies vaguely for the majority of the design points (between 50 W and 55 W), therefore **O3** may be disregarded in the decision making process when selecting a design point. This indicates that a similar actuator response is achievable using each of the four geometries, and therefore only **O1** vs. **O2** is shown separately. A trade off exist between the average actuator power and actuator core height. Naturally, designs with small actuator height demands larger actuator power and vice-versa. The average actuator power varies for most designs in the range 40-500 W while the actuator heights for most design are in the range 8-40 mm. It is worth noticing that, if a too small or inefficient actuator design is

used, the actuator power quickly exceeds the flow losses by several factors. The actuator height using geometry D is generally larger than for the remaining geometries. The results show similar Parato front's for geometry A and B.

The actuator prototype design is given by:

$$\vec{x} = (d_{\text{wire}}, h_{\text{coil}}, R, b_{\text{pm}}, h_{\text{core}}, h_{\text{air}}, V_{\text{supply}}, \theta_{\text{cl,L}}, \theta_{\text{cl,H}}, \Delta\theta_{\text{cl,L}}, \Delta\theta_{\text{cl,H}})$$

is

$$\vec{x} = (0.25\text{ mm}, 9.0\text{ mm}, 15.0\text{ mm}, 3.1\text{ mm}, 1\text{ mm}, 19.0\text{ mm}, 85\text{ V}, 59.2\text{ deg}, 234.8\text{deg}, 8.4\text{ deg}, 8.7\text{ deg})$$

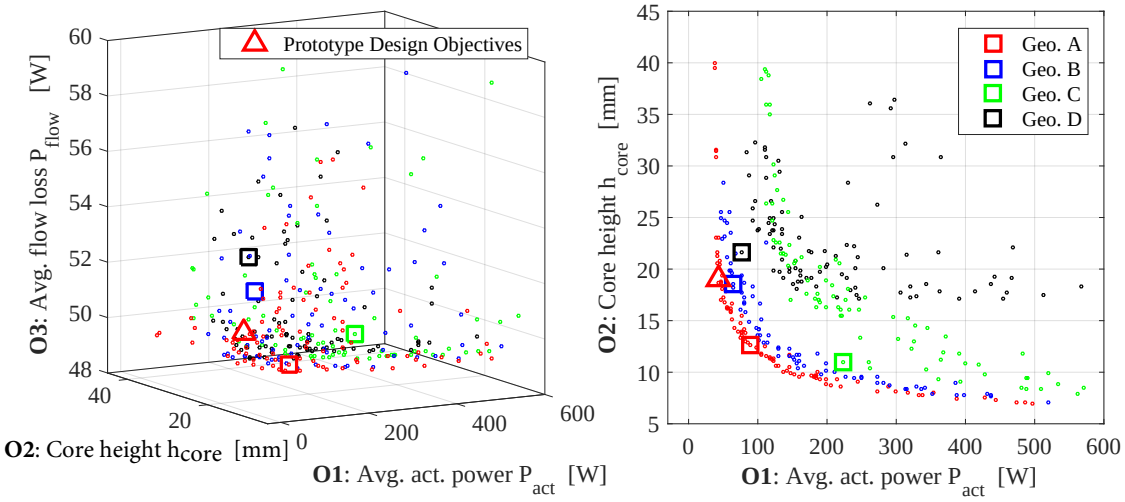

Figure 13: Optimization results using the four different actuator geometries. The minimum objective points for each design objective have been highlighted along with the design point of the actuator prototype.

Table 4: Magnetic and electrical properties of materials used in static electro-magnetic FEA.

Description	**Geo. A**	**Geo. B**	**Geo. C**	**Geo. D**
No. of objectives	3	3	3	3
No. of design variables	11	11	11	12
No. of constraints	6	7	7	9
Population size	100	100	100	100
No. generations	250	250	250	250
No. function evaluations	25k	25k	25k	25k
GDE3 control settings: CR,F	0.75,0.25	0.75,0.25	0.75,0.25	0.75,0.25
No. fronts in final generation	1	1	1	3
% of gen. in first front	100	100	100	30

6 CONCLUSIONS AND FUTURE WORK

Different moving coil actuator geometry topologies, for DDM's, have been explored through optimization. In total, four different permanent magnet placement have been tested to find the most suited topology. The objectives are to minimize the actuator height and actuator power and flow loss. Evaluation of the objectives include static-electro magnetic FEA and

lumped parameter models enabling simulation of entire DDM cycles. The optimization tool successfully converged towards a set of non-dominated solutions for each optimisation problem. The optimization result showed that the average flow losses only varies vaguely which indicates efficient machine operation is feasible using all of the proposed topologies. However, some geometries generally require more space than others, and some geometries requires larger actuator power. The most suited topologies are geometry A and B which both uses radially magnetized permanent magnets. An actuator and valve prototype has been manufactured based on the optimization results with a core height of 19 mm and an average actuator power 20 W, enabling an efficiency of 99.4 % during motoring operation (only valve related losses are considered). Future work involves experimental testing of the prototype to verify the models used in the optimization.

References

[1] Daniel Beck Roemer. *Design and Optimization of Fast Switching Valves for Large Scale Digital Hydraulic Motors*. PhD thesis, 2014.

[2] Daniel Roemer, Per Johansen, Henrik C. Pedersen, and Torben Ole Andersen. *Topology Selection and Analysis of Actuator for Seat Valves suitable for use in Digital Displacement Pumps/Motors*, pages 418–424. IEEE Press, 2013.

[3] S.H. Salter and W.H.S. Rampen. Pump control method and poppet valve therefor, March 2 1993. US Patent 5,190,446.

[4] S.H. Salter and W.H.S. Rampen. Improved fluid-working machine, July 15 1992. EP Patent App. EP19,900,915,148.

[5] J. Quilter. Mitsubishi to unveil 7MW offshore turbine. Wind Power Monthly, November 2011. Available at www.windpowermonthly.com.

[6] Kazuhisa Tsutsumi, Toshihide Noguchi, Yasuhiro Korematsu, Masayuki Shimizu, Alasdair Robertson, Uwe Stein, and Hauke Karstens. Hydraulic pump structure for wind turbine generator or tidal current generator and method of mounting hydraulic pump, November 28 2012. CN Patent App. CN 201,080,003,097.

[7] T. Kameda, M. Uchida, O. Uehara, H. Dodson, A. Robertson, and W. Rampen. Hydraulic pump, method for maintaining same, and wind power generation device, July 23 2014. EP Patent App. EP20,130,809,430.

[8] Salter Stephen, Stein Uwe, Dodson Henry, Fox Robert, Robertson Alasdair, and Mcgrath Tom. Method and apparatus for performing maintenance on hydraulic pump, and power generating apparatus of renewable energy type, May 8 2013. CN Patent App. CN 201,180,031,163.

[9] I. Haskara., V. V. Kokotovic, and L. A. Mianzo. Control of an electro-mechanical valve actuator for a camless engine. *International Journal of Robust and Nonlinear Control*, 14(6):561–579, 2004.

[10] Static performance of a polarized permanent-magnet reluctance actuator for internal combustion engine valve actuation. *IEEE Transactions on Magnetics*, 42(8):2063–2070, Aug 2006.

[11] B. Lequesne. Fast-acting long-stroke bistable solenoids with moving permanent magnets. *IEEE Transactions on Industry Applications*, 26(3):401–407, May 1990.

[12] Liang Liu and S. Chang. A moving coil electromagnetic valve actuator for camless engines. In *2009 International Conference on Mechatronics and Automation*, pages 176–180, Aug 2009.

[13] R. Storn and K. Price. Differential Evolution - A simple and efficient adaptive scheme for global optimization over continuous spaces. Tech. report TR-95-012, Berkeley, Cambridge, MA, May 1995.

[14] S. Kukkonen and J. Lampinen. Gde3: the third evolution step of generalized differential evolution. In *2005 IEEE Congress on Evolutionary Computation*, volume 1, pages 443–450 Vol.1, Sept 2005.

[15] S. Kukkonen. *Generalized Differential Evolution for Global Multi-Objective Optimization with Constraints*. PhD thesis, Lappeenranta University of Technology, 2012.

[16] D. Meeker. Finite element method magnetics, version 4.2, user's manual, 2015.

[17] W. L. Soong. Bh curve and iron loss measurements for magnetic materials, May 12 2008.

[18] J A Wagner. The shorted turn in the linear actuator of a high performance disk drive. *Magnetics, IEEE Transactions on*, 18(6):1770–1772, 1982.

[19] C. Noergaard, D. B. Roemer, and M. M. Bech. Modelling of moving coil actuators in fast switching valves suitable for digital hydraulic machines. In *Proc. of 2015 ASME Fluid Power and Motion Control*, Chicago, US, October 2015.

[20] Isaak D Mayergoyz. *Nonlinear Diffusion of Electromagnetic Fields*. Academic Press, 1998.

[21] D. B. Roemer, P. Johansen, L. Schmidt, and T. O. Andersen. Modeling of movement-induced and flow-induced fluid forces in fast switching valves. In *Proc. of 2015 International Conference on Fluid Power and Mechatronics*, Harbin, China, August 2015.

[22] S. Salter. Digital hydraulics for renewable energy. In *Proc. of World Renewable Energy Conference Aberdeen 2005*, Aberdeen, UK, 2005.

[23] G.S.Payne. Potential of digital displacement hydraulics for wave energy conversion. In *the 6th European Wave and Tidal Energy Conference*, Glasgow, UK, 2005.

[24] Robert Y. S. Lai and Lyle F. Mockros. The stokes-flow drag on prolate and oblate spheroids during axial translatory accelerations. *Journal of Fluid Mechanics*, 52:1–15, 3 1972.

[25] W. Borutzky, B. Barnard, and J. Thoma. An orifice flow model for laminar and turbulent conditions. *Simulation Modelling Practice and Theory*, 10(34):141 – 152, 2002.